Dispersion-Engineered Guided-Wave Resonators in Anisotropic Single-Crystal Substrates—Part I: Concept and Analytical Design

Mayur Ghatge, *Student Member, IEEE*, and Roozbeh Tabrizian, *Member, IEEE*

***Abstract*— This paper presents an analytical approach for the implementation of high quality-factor (Q) resonators with arbitrary cross-sectional vibration mode shapes in anisotropic single-crystal substrates. A closed-form dispersion relation is analytically derived to characterize the dynamics of guided waves in rectangular waveguides. Three categories of waves with propagating, standing-evanescent, and propagating-evanescent dynamics are identified and used for energy localization of acoustic excitations with arbitrary cross-sectional vibration patterns. An analytical design procedure is presented for dispersion engineering of waveguides to realize high-Q resonators without the need for geometrical suspension through narrow tethers or rigid anchors. The effectiveness of the dispersion engineering methodology is verified through the development of experimental test vehicles in 20-μm-thick single-crystal silicon substrate with 500-nm aluminum nitride transducers. Various proof-of-concept resonators, representing guided waves with different dispersion types, are presented and compared to highlight the optimum design procedures for Q enhancement and spurious mode suppression. Part I of this paper presents the operation principle of guided-wave resonators based on the analytical derivation of dispersion relation followed by a systematic resonator design procedure. Numerical and experimental characterizations for verification of the proposed design procedure and extensive measurement data on proof-of-concept resonators are presented in Part II.**

***Index Terms*— Acoustic energy localization, dispersion engineering, guided-wave dispersion anisotropic single-crystal substrate, high-Q, lamb wave dispersion, micromechanical resonator.**

I. INTRODUCTION

THE emerging 5G wireless communication systems target operation in multiband carrier aggregation schemes to fulfill the ever-growing need for higher data rates and communication capacity [1], [2]. To realize multiband wireless systems, there is an urgent need for high quality-factor (Q) resonator technology with lithographical frequency definition capability. These resonators enable single-chip integration of radio frequency front-end (RFFE) filters, and frequency references needed for configurable data communication over a wide frequency spectrum. Various micromechanical resonator technologies operating in in-plane vibration modes are introduced and developed over the past decade to provide the required lithographical frequency scalability [3]–[9]. Although capable to meet current RFFE requirements, these technologies fail to provide an analytical design methodology that sustains the major resonator performance metrics, i.e., high Q and electromechanical coupling coefficient (k_t^2), over extreme frequency scaling in ultra/super-high-frequency (UHF/SHF) regimes with current fabrication limitations.

To reduce the impact of Q degradation over extreme frequency scaling, a recent wave of research and development has targeted the use of single-crystal substrates and films that offer substantially lower acoustic dissipation compared to sputtered piezoelectric films, to enable the realization of high-performance filters, duplexers, and frequency references over and beyond the UHF regime [10]–[18]. Besides opting for low-loss substrates, a frequency scalable design strategy that enables uniform acoustic energy localization within the electromechanical transduction area is the fundamental requirement for the realization of resonators with high Q and k_t^2 over a wide spectrum of interest on a single chip.

Since the advent of in-plane micromechanical resonators, various design approaches targeting energy localization of bulk acoustic waves (BAW) in geometrically suspended microstructures to realize high-Q resonators have been demonstrated [3]–[6], [19]–[23]. Such localization is realized through definition of stress-free or fixed boundaries surrounding a released microstructure. In these approaches, the vibration mode shape must contain a naturally formed or an artificially forced nodal point, line, or face to facilitate anchoring the resonator to the surrounding substrate through narrow tethers or clamped surfaces. For resonators operating in the lateral mode of vibration, the resonance frequency is inversely proportional to lithographically defined dimensions. Therefore, radical frequency scaling of these resonators requires the proportional downscaling of the nodal tethers. In practice, the proportional miniaturization of narrow tethers connected to nodal points or formation of ideal rigid anchors for facial clamping is bounded by fabrication limitations such as lithography resolution or undercut in the cavity formation. Furthermore, these techniques are not systematically scalable to all resonators on the same substrate since changing the lateral frequency-defining dimensions, while having a constant thickness, induces substantial transformation of the vibration modes [24]. This transformation may exclude the desired nodal

---

Manuscript received January 18, 2019; accepted March 16, 2019. Date of publication March 22, 2019; date of current version June 5, 2019. This work was supported by the NSF under Grant ECCS 1752206. *(Corresponding author: Mayur Ghatge.)*

The authors are with the Electrical and Computer Engineering Department, University of Florida, Gainesville, FL 32611 USA (e-mail: ruyam@ufl.edu; rtabrizian@ufl.edu).

Digital Object Identifier 10.1109/TUFFC.2019.2907085

point or degrade electromechanical transduction efficiency, thus imposing the need for customized geometrical and transducer design for each desired frequency.

The first part of this paper presents an analytical methodology, based on dispersion characteristics of guided waves in anisotropic single-crystal substrates, which enables the systematic design of high-Q resonators with arbitrary cross-sectional mode shapes and frequencies. For the first time, the guided-wave dispersion relation is derived for rectangular waveguides implemented in anisotropic single-crystal substrates with the rectangular cross section. The identified dispersive propagating and evanescent waves can be used for designing high-Q and k_t^2 resonator through efficient energy localization without the need for geometrical suspension. The resulting dispersion-engineered resonators are anchored through wide tethers that encompass negligible mechanical energy density, hence, reducing anchoring energy leakage, while enhancing power handling and linearity [25]. Furthermore, such wide tethers enable the integration of multiple electrodes for simultaneous multimode excitation [26] or heterogeneous integration with transistors to realize the resonant body electronic components [27].

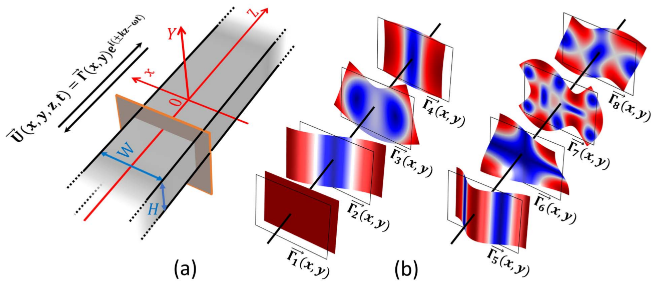

Fig. 1. (a) Infinitely long waveguide with rectangular cross section, extended in the z-direction. H and W are the height and width of the cross section of waveguide. (b) Cross-sectional mode patterns for different guided waves.

II. GUIDED-WAVE DISPERSION IN ANISOTROPIC SINGLE-CRYSTAL WAVEGUIDES

Harmonic excitations in an infinitely long waveguide with finite-cross-sectional dimensions are limited to a discrete set of propagating and standing waves, i.e., guided waves, with specific frequencies and wavenumbers. The linear superposition of guided waves at a specific frequency can form a vibration mode, when the waveguide is properly terminated at the two ends. Therefore, the identification of the guided waves and their dispersion characteristics (i.e., the relationship between their frequency and wavenumber) along with proper termination of the waveguide enables analytical synthesis of vibration modes.

For a waveguide with rectangular cross section implemented in an anisotropic single-crystal solid [Fig. 1(a)], wave propagation dynamics are governed by the equation of motion [28], limited by the stress-free boundary condition (B.C.) at the peripheral faces and is mathematically defined through

$$\left\{\begin{array}{l} \nabla.C:\nabla\vec{U}=\rho\dfrac{\partial^2\vec{U}}{\partial t^2} \\ \text{B.C.}(1):\sigma_{i=1,5,6}\left(\pm\dfrac{W}{2},y,z\right)=0 \\ \text{B.C.}(2):\sigma_{i=2,4,6}\left(x,\pm\dfrac{H}{2},z\right)=0 \end{array}\right\} \quad (1)$$

where $\vec{U}(x,y,z,t)$ is the 3-D displacement vector and $\nabla.$ is the divergence operator matrix defined by

$$\nabla.=\begin{bmatrix} \dfrac{\partial}{\partial x} & 0 & 0 & 0 & \dfrac{\partial}{\partial z} & \dfrac{\partial}{\partial y} \\ 0 & \dfrac{\partial}{\partial y} & 0 & \dfrac{\partial}{\partial z} & 0 & \dfrac{\partial}{\partial x} \\ 0 & 0 & \dfrac{\partial}{\partial z} & \dfrac{\partial}{\partial y} & \dfrac{\partial}{\partial x} & 0 \end{bmatrix} \quad (2)$$

where ∇ is the gradient matrix operator, which is the transpose of $\nabla.$ (i.e., $\nabla. = \nabla^T$). C is the elastic constant matrix for an arbitrary anisotropic material along major crystal axis, in the Voigt notation

$$C=\begin{bmatrix} c_{11} & c_{12} & c_{13} & 0 & 0 & 0 \\ c_{12} & c_{22} & c_{23} & 0 & 0 & 0 \\ c_{13} & c_{23} & c_{33} & 0 & 0 & 0 \\ 0 & 0 & 0 & c_{44} & 0 & 0 \\ 0 & 0 & 0 & 0 & c_{55} & 0 \\ 0 & 0 & 0 & 0 & 0 & c_{66} \end{bmatrix} \quad (3)$$

where c_{ij} coefficients are assumed to be real numbers. ρ is the mass density; $\sigma_i(i=1-6)$ are the components of stress vector in the Voigt notation; finally, H and W are the height and width of the cross section of the waveguide that is centrosymmetric to origin and extended in the z-direction (Fig. 1).

Equation (1) can be solved for displacement vectors of $\vec{U}=\vec{\Gamma}(x,y)e^{i(kz-\omega t)}$ to identify the cross-sectional vibration vector (i.e., $\vec{\Gamma}(x,y)=\begin{bmatrix} U_x(x,y) \\ U_y(x,y) \\ U_z(x,y) \end{bmatrix}$) and the corresponding frequency–wavenumber pair [i.e., (ω,k)] of the allowed harmonic and collective excitations in the waveguide. Such a solution set defines the dispersion characteristics of the guided waves.

The dispersion characteristics of the guided waves in isotopic plate waveguides (i.e., $W\rightarrow\infty$) can be analytically extracted using the displacement potentials [29]. In this approach, the propagation dynamics of extensional and shear constituents of the guided waves can be uncoupled, resulting in the straightforward derivation of a closed-form dispersion relation [29]. Unlike isotropic solids, in anisotropic waveguides, dynamics of extensional and shear waves are inherently coupled. Therefore, a similar approach is not applicable for the extraction of dispersion relation. This section presents the formulation for extraction of the dispersion relation for symmetric guided waves in waveguides implemented in anisotropic single-crystal substrates. The equation of motion in (1) is solved for the two extreme cases of plane strain (i.e., $H/W\rightarrow\infty$) and plane stress (i.e., $H/W\rightarrow 0$). These conditions reduce the complexity of wave dynamics and facilitate the derivation of closed-form dispersion relations.

A. Plane Strain

In the plane-strain case, the displacement in the y-direction nulls out. Therefore, the cross-sectional vibration vector is reduced to

$$\vec{\Gamma}(x,y)=\begin{bmatrix} U_x(x,y) \\ 0 \\ U_z(x,y) \end{bmatrix}.$$

Furthermore, the boundary condition of (1) is limited to $\sigma_{i=1,5,6}(\pm(W/2),y,z)=0$. Therefore, in the plane-strain case, (1) reduces to a system of two coupled complex differential equations

$$\left\{\begin{array}{l} \dfrac{\partial^2 U_x}{\partial x^2}+\left(\dfrac{\rho\omega^2-c_{55}k^2}{c_{11}}\right)U_x+\left(ik\dfrac{c_{13}+c_{55}}{c_{11}}\right)\dfrac{\partial U_z}{\partial x}=0 \\ \dfrac{\partial^2 U_z}{\partial x^2}+\left(\dfrac{\rho\omega^2-c_{33}k^2}{c_{55}}\right)U_z+\left(ik\dfrac{c_{13}+c_{55}}{c_{55}}\right)\dfrac{\partial U_x}{\partial x}=0 \end{array}\right\}. \tag{4}$$

The harmonic solution space for the system of differential equations in (4) includes the following symmetric cross-sectional vibration modes:

$$\left\{\begin{array}{l} U_x=f_1A_x\sin(p_1x)-if_2A_z\sin(p_2x) \\ U_z=if_3A_x\cos(p_1x)+f_4A_z\cos(p_2x) \end{array}\right\} \tag{5}$$

wherein, p_1 and p_2 are the characteristic roots defined by

$$(c_{11}p^2-\rho\omega^2+c_{55}k^2)(c_{55}p^2-\rho\omega^2+c_{33}k^2) = p^2k^2(c_{13}+c_{55})^2 \tag{6}$$

and f_i $(i=1\text{–}4)$ are related through

$$\left\{\begin{array}{l} \dfrac{f_1}{f_3}=\dfrac{\left(c_{55}p_1^2-\rho\omega^2+c_{33}k^2\right)}{p_1k(c_{13}+c_{55})} \\ \dfrac{f_2}{f_4}=\dfrac{\left(c_{55}p_2^2-\rho\omega^2+c_{33}k^2\right)}{p_2k(c_{13}+c_{55})} \end{array}\right\}. \tag{7}$$

Applying the boundary conditions at the stress-free peripheral faces of the waveguide (i.e., $\sigma_{i=1,5,6}$ $(\pm(W/2),y,z)=0$) to the solution in (5) yields (8) as shown at the bottom of this page. To have nonzero solutions for $\begin{bmatrix} A_x \\ A_z \end{bmatrix}$, (9) as shown at the bottom of this page, should hold true, which further yields the dispersion relation given by (10), as shown at the bottom of this page.

B. Plane Stress

In the plane-stress case, stress components in the y-direction are 0 (i.e., $\sigma_{i=2,4,6}$ $(x,\pm(H/2),z)=0$). Taking a similar approach to the plane-stress case for symmetric guided modes yields the dispersion relation given by (11) as shown at the bottom of this page. The complexity of dispersion relation in the anisotropic plate and waveguide is clear when compared to the isotropic plates, that is derived as [29]

$$\left\{\begin{array}{l} \dfrac{\tan\left(p_2\dfrac{W}{2}\right)}{\tan\left(p_1\dfrac{W}{2}\right)}=\dfrac{-4k^2p_1p_2}{\left(p_2^2-k^2\right)} \\ p_1=\dfrac{\rho\omega^2}{c_{11}}-k^2,\ p_2=\dfrac{\rho\omega^2}{(c_{11}-c_{12})/2}-k^2 \end{array}\right\}. \tag{12}$$

A MATLAB code, based on the bisection method [30], is used to extract the dispersion diagram [i.e., $(f=(\omega/2\pi), k)$] from (10) and (11). Fig. 2(a) and (b) demonstrates the extracted dispersion diagram for the first three branches of symmetric guided waves for plane-stress and plane-strain cases, for waveguides with 50-μm width and aligned to $\langle 100\rangle$ and $\langle 110\rangle$ crystallographic orientation of (100) silicon plate. It is evident that apart from the S_0 guided waves that originate at $(f,k)=(0,0)$, other symmetric modes

$$\begin{bmatrix} (c_{11}f_1p_1-c_{13}f_3k)\cos\left(\pm p_1\dfrac{W}{2}\right) & i(-c_{11}f_2p_2+c_{13}f_4k)\cos\left(\pm p_2\dfrac{W}{2}\right) \\ i(f_1k-f_3p_1)\sin\left(\pm p_1\dfrac{W}{2}\right) & (f_1k-f_4p_2)\sin\left(\pm p_2\dfrac{W}{2}\right) \end{bmatrix}\begin{bmatrix} A_x \\ A_z \end{bmatrix}=\begin{bmatrix} 0 \\ 0 \end{bmatrix} \tag{8}$$

$$\det\begin{bmatrix} (c_{11}f_1p_1-c_{13}f_3k)\cos\left(\pm p_1\dfrac{W}{2}\right) & i(-c_{11}f_2p_2+c_{13}f_4k)\cos\left(\pm p_2\dfrac{W}{2}\right) \\ i(f_1k-f_3p_1)\sin\left(\pm p_1\dfrac{W}{2}\right) & (f_2k-f_4p_2)\sin\left(\pm p_2\dfrac{W}{2}\right) \end{bmatrix}=0 \tag{9}$$

$$\frac{\tan\left(p_2\frac{W}{2}\right)}{\tan\left(p_1\frac{W}{2}\right)}=\frac{(c_{11}f_2p_2-c_{13}f_4k)(f_2k-f_3p_1)}{(c_{11}f_1p_1-c_{13}f_3k)(f_1k-f_4p_2)} \tag{10}$$

$$\left\{\begin{array}{l} \dfrac{\tan\left(p_2\frac{W}{2}\right)}{\tan\left(p_1\frac{W}{2}\right)}=\dfrac{\left(\left(c_{11}-\frac{c_{13}^2}{c_{11}}\right)f_2p_2-\left(c_{13}+c_{55}-\frac{c_{13}^2}{c_{11}}\right)f_4k\right)(f_2k-f_3p_1)}{\left(\left(c_{11}-\frac{c_{13}^2}{c_{11}}\right)f_1p_1-\left(c_{13}+c_{55}-\frac{c_{13}^2}{c_{11}}\right)f_3k\right)(f_1k-f_4p_2)} \\ \left(\left(c_{11}-\dfrac{c_{13}^2}{c_{11}}\right)p^2-\rho\omega^2+c_{55}k^2\right)\left(c_{55}p^2-\rho\omega^2+\left(c_{33}-\dfrac{c_{13}^2}{c_{33}}\right)k^2\right)=p^2k^2\left(c_{13}+c_{55}-\dfrac{c_{13}^2}{c_{33}}\right)\left(c_{13}+c_{55}-\dfrac{c_{13}^2}{c_{11}}\right) \\ \dfrac{f_1}{f_3}=\dfrac{\left(\left(c_{13}+c_{55}-\frac{c_{13}^2}{c_{11}}\right)p_1^2-\rho\omega^2+\left(c_{33}-\frac{c_{13}^2}{c_{33}}\right)k^2\right)}{p_1k\left(c_{13}+c_{55}-\frac{c_{13}^2}{c_{11}}\right)},\quad \dfrac{f_2}{f_4}=\dfrac{\left(\left(c_{13}+c_{55}-\frac{c_{13}^2}{c_{11}}\right)p_2^2-\rho\omega^2+\left(c_{33}-\frac{c_{13}^2}{c_{33}}\right)k^2\right)}{p_2k\left(c_{13}+c_{55}-\frac{c_{13}^2}{c_{11}}\right)} \end{array}\right\} \tag{11}$$

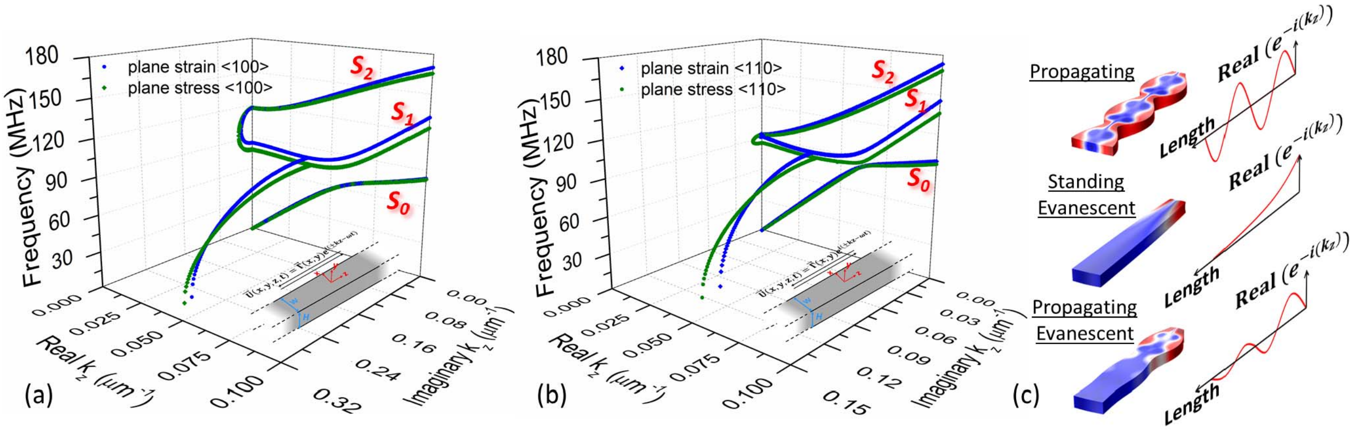

Fig. 2. Extracted dispersion characteristics for the three symmetric modes in a waveguide with 50-μm width, for plane-stress and plane-strain cases in (a) $\langle 100\rangle$ and (b) $\langle 110\rangle$ crystallographic orientation of (100) single-crystal silicon (SCS) substrate. Apart from the propagating waves with real wavenumber ($k_z = k$; $k \in \mathbb{R}$), S_1 and S_2 have standing-evanescent waves with pure imaginary wave numbers ($k_z = ik$; $k \in \mathbb{R}$). S_1 has an additional branch of propagating-evanescent wave with complex wavenumbers ($k_z = k_1 + ik_2$; k_1 and $k_2 \in \mathbb{R}$) originating from the zero-group velocity point of the branch. (c) Corresponding vibration mode shapes to the propagating, standing-evanescent, and propagating-evanescent waves for S_1 branch, along with their axial propagation function across the waveguide length.

have imaginary and/or complex wavenumbers. Also, it is worth noting that while S_0 and S_2 follow type-I dispersion characteristics, S_1 exhibits type-II dispersion characteristics up to the guided wave with zero-group velocity (i.e., $k = k_{\mathrm{ZG}}$ where $(\partial f/\partial k)|_{k=k_{ZG}} = 0$). For S_1 guided waves with $k > k_{\mathrm{ZG}}$, S_1 manifests type-I dispersion [31], [32]. Finally, there exist an extension to the S_1 branch, originating from k_{ZG}, which represents wavenumbers with complex values (called complex branch, hereafter) and meets $f = 0$ plane perpendicularly. Therefore, the extraction of the guided waves dispersion characteristics in anisotropic single-crystal waveguides identifies three categories of propagating and evanescent solutions: 1) the propagating waves with real wavenumber $k = k_{\mathrm{real}}$; 2) standing-evanescent waves with purely imaginary wavenumber $k = ik_{\mathrm{imag}}$; and 3) propagating-evanescent waves with complex wavenumbers $k = k_{\mathrm{real}} + ik_{\mathrm{imag}}$. Considering imaginary c_{ij} coefficients in (3) and, thus, the dissipation constants alters the evanescent wave solutions but for the ease of analysis and constraining to the scope of discussion of the paper, we assume c_{ij} coefficients to be real numbers. The displacement function of these three categories is schematically shown in Fig. 2(c). The existence of evanescent solutions provides an acoustic means for the energy localization without the need for geometrical suspension as shown previously for thickness modes [33], [34]. Section III presents an analytical design procedure for synthesis of high-Q resonators using propagating and evanescent guided waves in anisotropic waveguides.

III. DISPERSION ENGINEERING FOR ACOUSTIC ENERGY LOCALIZATION

As evident in dispersion diagrams shown in Fig. 2, the S_0 branch initiates from the origin of (ω, k) space, while branches to other waves originate at ($\omega \neq 0$, $k_{\mathrm{BAW}} = 0$). While most branches include both propagating (i.e., $k \in \mathbb{R}$) and standing-evanescent (i.e., $ik \in \mathbb{R}$) sections, in some cases, such as the S_1 branch, there exists an extension representing propagating-evanescent waves with complex wavenumber (i.e., $k = k_1 + ik_2$; k_1 and $k_2 \in \mathbb{R}$).

A set of guided waves with different cross-sectional patterns, $\vec{\Gamma}_i(x, y)$, can be simultaneously excited at a specific frequency to form a standing vibration mode. In a generic definition, a 3-D standing vibration mode, $\vec{\Gamma}(x, y, z, t)$, is created through the linear superposition of bidirectional propagating and propagating-evanescent waves, in addition to standing-evanescent waves

$$\begin{aligned}\vec{\Gamma}(x, y, z, t) &= \mathrm{Re}\Bigg\{\sum_m A_m \vec{\Gamma}_m(x, y)[e^{i(k_m z-\omega t)} + e^{i(-k_m z-\omega t)}] + \sum_n B_n \\ &\qquad \vec{\Gamma}_n(x, y)e^{-k_n z}e^{i(-\omega t)} + \sum_p B_p \vec{\Gamma}_p(x, y)e^{k_p z}e^{i(-\omega t)}\Bigg\}\end{aligned} \tag{13}$$

where A_m and $B_{n,p}$ are the weighting coefficients for the propagating/propagating-evanescent and standing-evanescent waves, respectively, and are defined by the excitation scheme (i.e., distribution and placement of excitation sources). The weighting coefficients can be engineered with proper transduction schemes and waveguide termination strategies to ensure the suppression of undesired guided waves or reduce their corresponding amplitude, thus limiting the excitations to a specific guided wave with desired cross-sectional pattern. In this case, (13) can be simplified to

$$\vec{\Gamma}_i(x, y, z, t) = \vec{\Gamma}_i(x, y)\Psi_i(z)\cos(\omega t) \tag{14}$$

where $\Psi_i(z)$ is the generalized axial mode shape defined by

$$\Psi_i(z) = A_i \cos(k_{i,1} z) + B_i e^{-k_{i,2} z} + C_i \cos(k_{i,3} z)e^{-k_{i,4} z} \tag{15}$$

wherein, $k_{i,1}$, $ik_{i,2}$, and $k_{i,3} + ik_{i,4}$ are the wavenumbers of the propagating, standing-evanescent, and propagating-evanescent

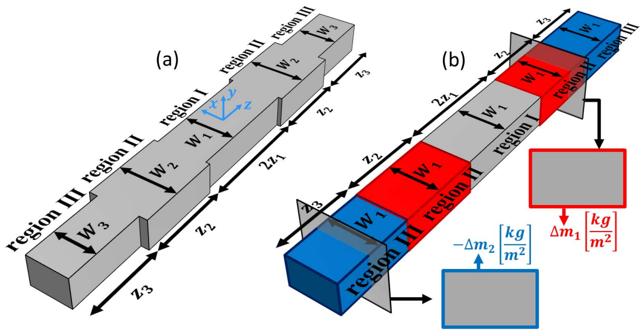

Fig. 3. Dispersion-engineered waveguide composed from three regions with different dispersion characteristics realized by (a) changing the width and (b) adding/removing surface mass, across the length. The changing in width or material composition transforms the corresponding dispersion characteristics of the constituent regions and limits the solution space for harmonic excitations through imposing additional boundary conditions.

guided waves corresponding to the dispersion branch of interest, at frequency ω. Also, depending on the extension of the corresponding dispersion branch in the (ω, k) space, one or all the weighting constants may vanish and are chosen to localize the desired mode shape in the waveguide. Finally, (15) assumes the placement of a centrosymmetric excitation source at the origin.

While the axial mode shape $\Psi_i(z)$ is extended infinitely over the length of the waveguide, realization of a high-Q resonance mode requires energy localization in a finite length. This can be achieved through engineering the dispersion characteristics of the waveguide across its length, to nullify the weighting coefficient corresponding to propagating waves [i.e., A in (15)] in regions alongside the excitation source.

The dispersion characteristics of the guided waves depend on the elastic properties and mass density of the constituting materials, as well as the cross-sectional geometry of the waveguide. Therefore, any change in the cross-sectional dimensions or material composition results in a transformation of the dispersion curves. Fig. 3 schematically demonstrates the dispersion-engineered waveguides that are created by the variation of the cross-sectional dimensions or the introduction of peripheral mass-loading, across the length.

To formulate the guided-wave dynamics, a dispersion-engineered waveguide can be interpreted as a set of rectangular waveguides with finite length that are acoustically coupled by cascading them in the length direction. This coupling significantly limits the solution space for harmonic excitations by imposing additional boundary conditions to the constituent waveguides. The additional boundary conditions are the continuity of particle displacement and strain at the transitional faces between cascaded waveguides. Considering an appropriate design that satisfies the boundary conditions, an axial mode-shape function $\Psi_i(z)$ of dispersion-engineered waveguides shown in Fig. 3 can be formulated by

$$\Psi_i(z) = \left\{ \begin{array}{ll} K_1\Psi_{i,1}(|z|) & z \in \text{Region I} \\ K_2\Psi_{i,2}(|z| - z_1) & z \in \text{Region II} \\ K_3\Psi_{i,3}(|z| - z_1 - z_2) & z \in \text{Region III} \end{array} \right\} \quad (16)$$

wherein, $\Psi_{i,1-3}(z)$ are the individual axial mode-shape functions corresponding to constituent waveguides (i.e., regions I, II, and III) defined by (15) and K_{1-3} are the constants necessary to meet strain and displacement boundary conditions at the interfaces of these individual waveguides.

Proper dispersion engineering of the waveguide can result in the creation of vibration modes $\Psi_i(z)$ with evanescent constituents in regions II and/or III. Such modes benefit from the exponential decay in the axial mode-shape functions across the length, which enables the acoustic energy localization in region I and without the need for geometrical suspension. This technique has been previously demonstrated in thickness-mode aluminum nitride (AlN) BAW resonators for enhancement of $k_t^2 Q$ and suppression of spurious modes, through engineering waveguide stack (i.e., addition of metallic border rings) [31]–[35].

In this paper, the required dispersion engineering is achieved through changing the width of the waveguide across its length. Unlike thickness-mode counterparts where dispersion characteristics of the concerned guided wave vary with thickness variation, the dispersion characteristics of guided waves with the in-plane cross-sectional vibration pattern vary with respect to the changes in the waveguide width. Therefore, the desired dispersion engineering for acoustic energy localization can be achieved through the simple lithographical variation of the waveguide geometry without the need for addition of a new material.

Depending on the dispersion type of the corresponding guided wave, different engineering strategies can be used to create high-Q resonance modes. In this section, two extensional guided waves with different dispersion types are used to demonstrate the energy localization and analytical mode synthesis concept. Fig. 4(a) and (b) demonstrates the dispersion characteristics of the third and first width-extensional (WE) guided waves, respectively, for waveguides with different widths (i.e., $W_3 < W_1 < W_2$) and 20-μm thickness. As evident, WE$_3$ wave manifests dispersion type-I, while WE$_1$ wave shows both type-II and type-I dispersion characteristics. Guided waves with group velocity ($v_g = \delta\omega/\delta k > 0$) are known to demonstrate type-I dispersion characteristics, while guided waves with ($v_g < 0$) demonstrate type-II dispersion characteristics. As shown in Fig. 4(b), WE$_1$ wave demonstrates type-I as well as type-II dispersion.

A. Type-I Dispersion Engineering

For the guided waves with dispersion type-I [Fig. 4(a)], acoustic energy localization can be achieved through enforcing the excitation of a standing-evanescent solution in region III at the desired operation frequency f_0, thus yielding an exponentially decaying axial mode-shape function (i.e., $\Psi_{i,3}(|z|) = e^{-k_{i,3}(|z|-z_1-z_2)}$, $z \in$ Region III). Furthermore, to ensure a uniform energy distribution in region I, where the transducer will be placed, the waveguide geometry should be engineered to enforce the excitation of guided wave with infinitely long wavelength (i.e., $k = 0$) in region I, thus yielding a constant mode-shape function (i.e., $\Psi_{i,1}(|z|) = 1$). This ensures the realization of a "piston-shaped" vibration mode at desired frequency f_0. Benefiting from the uniform energy distribution in the active transduction region, resonators with piston-shaped

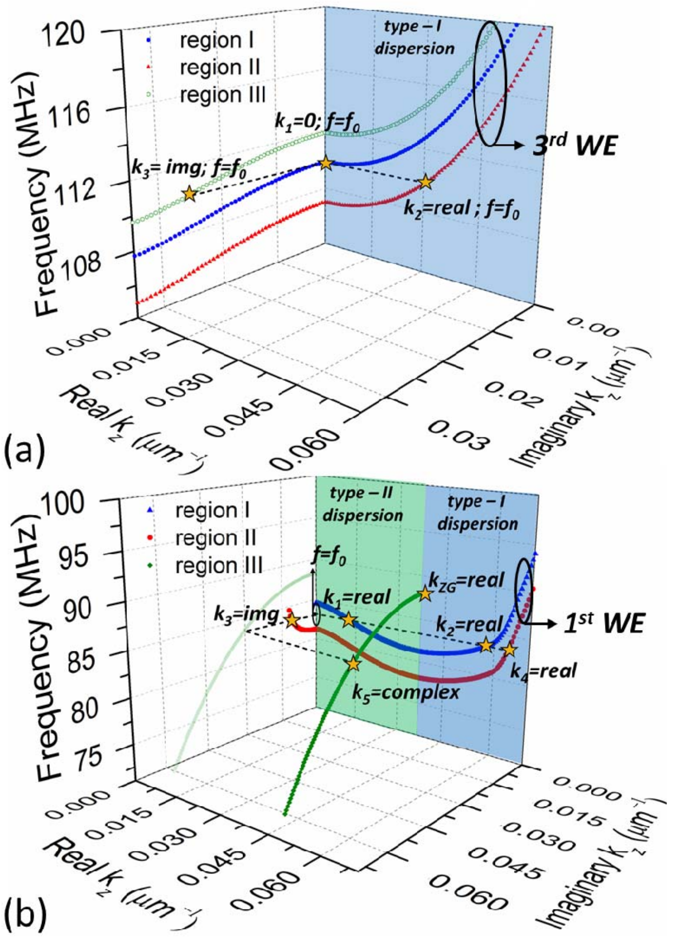

Fig. 4. Dispersion characteristics for guided waves exhibiting (a) type-I dispersion and (b) type-II and type-I dispersive characteristics. Changing the width of the waveguide (Fig. 3) transforms the dispersion characteristics of guided waves. The dispersion curves for S_1 wave are demonstrated for the three regions of the dispersion-engineered waveguide demonstrated in Fig. 3. The cross-plane at frequency f_0 intersects dispersion branches at various points, highlighted by stars. These points correspond to propagating, standing-evanescent, and propagating-evanescent guided waves in regions I–III. The complex-k dispersion characteristics of region III (shown in green) originates from the zero-group velocity point (k_{ZG}) of its corresponding real-k dispersion characteristics branch.

vibration modes provide enhanced k_t^2 and power handling [35]. Finally, to satisfy the required displacement and strain continuity across the waveguide, $\Psi_{i,1}$ and $\Psi_{i,3}$ should be coupled through a propagating wave with finite wavelength (i.e., $0 < k_2 \in \mathbb{R}$) in region II [i.e., $\Psi_{i,2} = \cos(k_{i,2})$].

The analytical design procedure for the synthesis of such vibration mode at frequency f_0 consists of identification of the width and length of constituting regions (i.e., regions I, II, and III). While the width of region I (i.e., W_1) must be defined to ensure the existence of a guided wave with $k = 0$, the choice of W_2 and W_3 should only suffice the existence of propagating and standing-evanescent waves at f_0. The axial mode-shape function of the dispersion-engineered waveguide can be written as

$$\Psi_{\mathrm{WE}_3}(z) = \left\{ \begin{array}{ll} K_1 & z \in \mathrm{I} \\ K_2 \cos(k_{\mathrm{WE}_3,2}(|z| - z_1)) & z \in \mathrm{II} \\ K_3 e^{-k_{\mathrm{WE}_3,3}(|z|-z_1-z_2)} & z \in \mathrm{III} \end{array} \right\} \quad \text{(17-a, b, c)}$$

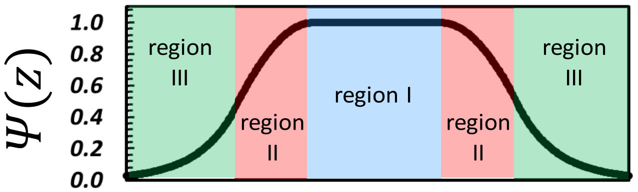

Fig. 5. Axial mode-shape function for the synthesized vibration mode with type-I dispersion characteristics.

where K_1, K_2, and K_3 are the vibration amplitudes and $k_{\mathrm{WE}_3,2}$ and $ik_{\mathrm{WE}_3,3}$ are the corresponding wavenumbers for the guided wave at f_0 in regions II and III, respectively. $2z_1$, z_2, and z_3 denote the lengths of regions I, II, and III in the engineered waveguide, with the origin for (17) being the center of the device (Fig. 3).

Considering (17-b) and (17-c), the displacement continuity at the interface of regions II and III (i.e., $z = z_1 + z_2$) requires

$$K_2 \cdot \cos(k_{\mathrm{WE}_3,2}(z_2)) = K_3. \tag{18}$$

Similarly, the continuity of strain at the interface of regions II and III requires

$$K_2 \cdot k_{\mathrm{WE}_3,2} \sin(k_{\mathrm{WE}_3,2}(z_2)) = K_3 \cdot k_{\mathrm{WE}_3,3}. \tag{19}$$

These systems of equations [(18) and (19)] result in a closed-form solution to calculate the length of region II as

$$z_2 = \frac{1}{k_{\mathrm{WE}_3,2}} \tan^{-1}\left(\frac{k_{\mathrm{WE}_3,3}}{k_{\mathrm{WE}_3,2}}\right). \tag{20}$$

The length of region III (i.e., z_3) is not derived from a closed-form equation and is chosen appropriately long to help in the sufficient decay of the energy profile, thus realizing the energy localization in region I, without the need for geometrical suspension. Fig. 5 demonstrates the axial mode shape for the "piston-shaped" mode realized using dispersion engineering for WE_3 guided wave with type-I dispersion.

Finally, it is worth noting that in the piston-shaped mode, the length of central region (i.e., $2z_1$) is a degree of freedom and can be chosen depending on the requirement of transduction area or limitations for the overall form factor of the device.

B. Type-II Dispersion Engineering

In theory, a similar strategy as discussed in Section III-A can be used to create "piston-shaped" modes for guided waves with type-II dispersion. However, opting for this approach in single-crystal silicon (SCS) waveguides is challenging considering the limited range of wavenumbers in the standing-evanescent section of the S_1 branch. Fig. 6 shows the comparison of the standing-evanescent branches of AlN and $\langle 110 \rangle$ silicon plates with similar frequencies of S_1 wave at $k = 0$. It is evident that the maximum wavenumber in the standing-evanescent section in $\langle 110 \rangle$ silicon is $|k_{\max,\mathrm{Si}}| \cong 0.0024\ \mu\mathrm{m}^{-1}$, which is significantly smaller in magnitude compared to that of AlN (i.e., $|k_{\max,\mathrm{AlN}}| \cong 0.0082\ \mu\mathrm{m}^{-1}$). Such a small wavenumber translates to the slow rate of exponential decay in the amplitude of axial mode-shape function $\Psi(z)$ and imposes

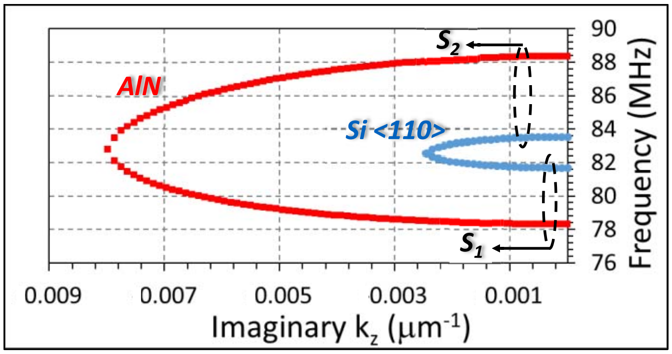

Fig. 6. Comparison of the dispersion characteristics of standing-evanescent S_1 waves in AlN and Si ⟨110⟩ plates with similar frequencies at $k = 0$. The maximum value for k in Si ⟨110⟩ is nearly four times smaller compared to AlN counterpart.

the need for very long flanks (i.e., region III waveguides) to sufficiently attenuate the acoustic energy density at the anchoring regions. Also, unlike the type-I case where region III can only support a standing-evanescent wave at f_0, in type-II dispersion characteristic, the standing-evanescent waves are accompanied by propagating wave with large wavenumbers. This can be observed in Fig. 4(b) where a cut-plane at f_0 intersects the dispersion branch corresponding to region III in two points with real and imaginary wavenumbers. These points highlighted through stars correspond to propagating and evanescent guided waves at f_0. The excitation of a propagating wave in region III is highly undesirable as it results in energy leakage out of active region I and reduces the resonator Q. Furthermore, anchoring/terminating region III at any point over its length leads to the destructive reflection of the propagating wave back into active region I. This reflection induces ripples in the axial mode-shape function in region I, hence resulting in degradation of k_t^2 and power handling.

To surpass these challenges, an alternative energy localization technique can be used through exploiting the propagating-evanescent extension of the S_1 branch (i.e., $k = k_1 + ik_2$; k_1 and $k_2 \in \mathbb{R}$). In this technique, a propagating wave with small wavenumber in region I is coupled to a propagating-evanescent wave in region III, through a standing-evanescent wave in region II, thus resulting in a unique vibration mode with efficient energy localization.

Opting for proper width on region III, the dispersion characteristics of the guided wave can be engineered to have a complex wavenumber with large imaginary part at the desired frequency f_0. Benefiting from much large imaginary part compared to standing-evanescent counterpart, propagating-evanescent waves enable the energy localization in small form factors in an SCS waveguides. Furthermore, the essential nature of propagating-evanescent waves facilitates the formation of nodal points that may further help to reduce the overall length of region III, while sustaining a high Q. Fig. 4(b) demonstrates the respective dispersion characteristics of the first WE guided wave in ⟨100⟩ silicon waveguides with different widths (i.e., $W_3 < W_1 < W_2$) that represents type-II and type-I dispersion.

The analytical design procedure to realize a resonator at frequency f_0 consists of the identification of the width and length of constituting regions I–III. Similar to dispersion type-I counterparts, W_2 should be chosen to ensure the existence of standing-evanescent wave at f_0. Also, W_3 should be chosen to enforce the f_{ZG} of S_1 branch to be larger than f_0, thus ensuring the existence of propagating-evanescent solution in region III at f_0. The axial mode-shape function ($\Psi_{WE_1}(z)$) for the dispersion-engineered resonator operating in the WE_1 mode can be written as

$$\begin{Bmatrix} K_1 \cos(k_{WE_1,1} z) & z \in \mathrm{I} \\ K_2 e^{-k_{WE_1,2}(|z|-z_1)} & z \in \mathrm{II} \\ K_3 e^{-k_{WE_1,3}(|z|-z_1-z_2+z_0)} & \\ \quad \times \cos(k_{ZG,3}(|z|-z_1-z_2+z_0)) & z \in \mathrm{III} \end{Bmatrix} \quad \text{(21-a, b, c)}$$

where K_1, K_2, and K_3 are the vibration amplitudes and $k_{WE_1,1}$, $ik_{WE_1,2}$, and $k_{ZG,3} + ik_{WE_1,3}$ are the corresponding wavenumbers for the guided waves at f_0 in regions I, II, and III, respectively. z_0 is the auxiliary correction term to facilitate appropriate displacement and strain continuity over the waveguide length.

Considering (21-a) and (21-b), the displacement continuity at the interface of regions I and II (i.e., $z = z_1$) requires

$$K_1 \cdot \cos\left(k_{WE_1,1}(z_1)\right) = K_2. \tag{22}$$

Similarly, the continuity of strain at the interface of regions I and II requires

$$K_1 \cdot k_{WE_1,1} \sin\left(k_{WE_1,2}(z_1)\right) = K_2 \cdot k_{WE_1,2}. \tag{23}$$

These systems of equations [(22) and (23)] result in a closed-form solution to calculate the length of region I as

$$z_1 = \frac{1}{k_{WE_1,1}} \tan^{-1}\left(\frac{k_{WE_1,2}}{k_{WE_1,1}}\right). \tag{24}$$

Considering (21-b) and (21-c), the displacement continuity at the interface of regions II and III (i.e., $z = z_1 + z_1$) requires

$$K_2 e^{-k_{WE_1,2}(z_2)} = K_3 e^{-k_{WE_1,3}(z_0)} \cos(k_{ZG,3} z_0). \tag{25}$$

Similarly, the continuity of strain at the interface of regions II and III requires

$$\begin{aligned} K_2 \cdot k_{WE_1,2} e^{-k_{WE_1,2}(z_2)} &\\ = K_3 \cdot e^{-k_{WE_1,3}(z_0)} k_{WE_1,3} \cos(k_{ZG,3} z_0) &\\ + K_3 \cdot e^{-k_{WE_1,3}(z_0)} k_{ZG,3} \sin(k_{ZG,3} z_0). & \end{aligned} \tag{26}$$

Replacing (24) in (25), z_0 can be calculated from

$$z_0 = \frac{1}{k_{ZG,3}} \tan^{-1}\left(\frac{k_{WE_1,2} - k_{WE_1,3}}{k_{ZG,3}}\right). \tag{27}$$

Also, considering (25) and (26), it is worth noting that the there is no unique solution for z_2; i.e., for any z_2 value, there exists a vibration amplitude K_3 to guarantee (25) and (26) hold.

Finally, z_3 is defined to benefit from the inherent nodal points of the propagating-evanescent guided wave in region III as

$$k_{ZG,3}(z_3 + z_0) = n\pi/2. \tag{28}$$

Such a z_3 ensures a zero displacement at the termination face of the waveguide, where it is anchored to the substrate.

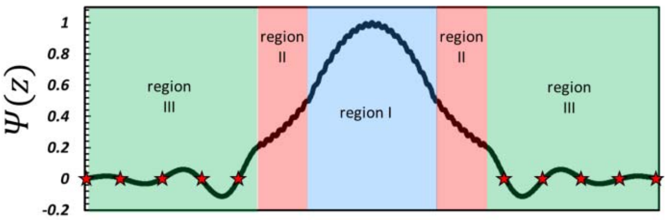

Fig. 7. Axial mode-shape function for the synthesized vibration mode with type-II and type-I dispersion characteristics. Nodal points in region III are marked in red stars.

It is worth noting that the proposed analytical design procedure for type-II dispersion targets the energy localization through both evanescent waves in regions II and III, as well as geometrical suspension (i.e., nodal point) in region III further enhancing Q. The relative contribution of each of these techniques in the efficiency of energy localization and resonator Q can be deliberately controlled by z_2. Propagating waves with large wavenumbers are in regions I and II are ignored in (21) for the ease of analytical derivation of the closed-form solution. Numerical methods can be used to solve resulting equations considering waves with large wavenumbers. Fig. 7 demonstrates the resulting axial mode-shape function of the mode having type-II dispersion characteristics.

The experimental methodology for the verification of design procedure and extensive measurement data on proof-of-concept resonators is presented in Part II.

REFERENCES

[1] G. G. Fattinger, "Carrier aggregation and its challenges-or: The golden age for acoustic filters," in *IEDM Tech. Dig.*, May 2016, pp. 1–4.

[2] R. Ruby, "A snapshot in time: The future in filters for cell phones," *IEEE Microw. Mag.*, vol. 16, no. 7, pp. 46–59, Aug. 2015.

[3] G. Piazza, P. J. Stephanou, and A. P. Pisano, "Piezoelectric aluminum nitride vibrating contour-mode MEMS resonators," *J. Microelectromech. Syst.*, vol. 15, no. 6, pp. 1406–1418, Dec. 2006.

[4] C. Cassella, Y. Hui, Z. Qian, G. Hummel, and M. Rinaldi, "Aluminum nitride cross-sectional Lamé mode resonators," *J. Microelectromech. Syst.*, vol. 25, no. 2, pp. 275–285, 2016.

[5] C.-M. Lin, Y.-J. Lai, J.-C. Hsu, Y.-Y. Chen, D. G. Senesky, and A. P. Pisano, "High-Q aluminum nitride Lamb wave resonators with biconvex edges," *Appl. Phys. Lett.*, vol. 99, no. 14, p. 143501, 2011.

[6] R. Abdolvand, H. M. Lavasani, G. K. Ho, and F. Ayazi, "Thin-film piezoelectric-on-silicon resonators for high-frequency reference oscillator applications," *IEEE Trans. Ultrason., Ferroelectr., Freq. Control*, vol. 55, no. 12, pp. 2596–2606, Dec. 2008.

[7] T.-T.Yen, A. P. Pisano, and C. T.-C. Nguyen, "High-Q capacitive-piezoelectric AlN lamb wave resonators," in *Proc. IEEE 26th Int. Conf. Micro Electro Mech. Syst. (MEMS)*, Jan. 2013, pp. 114–117.

[8] R. H. Olsson, III, "A high electromechanical coupling coefficient SH0 lamb wave lithium niobate micromechanical resonator and a method for fabrication," *Sens. Actuators A, Phys.*, vol. 209, Mar. 2014, pp. 183–190.

[9] S. Gong, and G. Piazza, "Design and analysis of lithium–niobate-based high electromechanical coupling RF-MEMS resonators for wideband filtering," *IEEE Trans. Microw. Theory Techn.* vol. 61, no. 1, pp. 403–414, Jan. 2013.

[10] J. B. Shealy *et al.*, "Low loss, 3.7 GHz wideband BAW filters, using high power single crystal AlN-on-SiC resonators," in *IEDM Tech. Dig.*, Jun. 2017, pp. 1476–1479.

[11] Y. Yang, A. Gao, R. Lu, and S. Gong, "5 GHz lithium niobate MEMS resonators with high FoM of 153," in *Proc. IEEE 30th Int. Conf. Micro Electro Mech. Syst. (MEMS)*, Jan. 2017, pp. 942–945.

[12] F. V. Pop, A. S. Kochhar, G. Vidal-Alvarez, and G. Piazza, "Laterally vibrating lithium niobate MEMS resonators with 30% electromechanical coupling coefficient," in *Proc. IEEE 30th Int. Conf. Micro Electro Mech. Syst. (MEMS)*, Jan. 2017, pp. 966–969.

[13] W. Pan, V. A. Thakar, M. Rais-Zadeh, and F. Ayazi, "Acoustically coupled thickness-mode AIN-on-Si band-pass filters—Part I: Principle and devices," *IEEE Trans. Ultrason., Ferroelectr., Freq. Control*, vol. 59, no. 10, pp. 2262–2269, Oct. 2012.

[14] R. Abdolvand, and F. Ayazi, "Monolithic thin-film piezoelectric-on-substrate filters," in *IEEE MTT-S Int. Microw. Symp. Dig.*, Jun. 2007, pp. 509–512.

[15] A. Ansari, V. J. Gokhale, V. A. Thakar, J. Roberts, and M. Rais-Zadeh, "Gallium nitride-on-silicon micromechanical overtone resonators and filters," in *IEDM Tech. Dig.*, Dec. 2011, pp. 20.3.1–20.3.4.

[16] H. W. Then, S. Dasgupta, and M. Radosavljevic, "Film bulk acoustic resonator (FBAR) devices for high frequency RF filters," U.S. Patent 20 180 323 767 A1, Dec. 4, 2015.

[17] L. C. Popa and D. Weinstein, "L-band lamb mode resonators in gallium nitride MMIC technology," in *Proc. IEEE Int. Freq. Control Symp. (FCS)*, May 2014, pp. 1–4.

[18] C. M. Lin, Y. Y. Chen, V. V. Felmetsger, D. G. Senesky, and A. P. Pisano, "AlN/3C-SiC composite plate enabling high-frequency and high-Q micromechanical resonators," *Adv. Mater.*, vol. 24, no. 20, pp. 2722–2727, 2012.

[19] C. Tu and J. Lee, "VHF-band biconvex AlN-on-silicon micromechanical resonators with enhanced quality factor and suppressed spurious modes," *J. Micromech. Microeng.*, vol. 26, no. 6, p. 065012, 2016.

[20] A. K. Samarao, G. Casinovi, and F. Ayazi, "Passive TCF compensation in high Q silicon micromechanical resonators," in *Proc. IEEE 23rd Int. Conf. Micro Electro Mech. Syst. (MEMS)*, Jan. 2010, pp. 116–119.

[21] M. Shahmohammadi, B. P. Harrington, and R. Abdolvand, "Concurrent enhancement of Q and power handling in multi-tether high-order extensional resonators," in *IEEE MTT-S Int. Microw. Symp.*, May 2010, pp. 1452–1455.

[22] B. P. Harrington and R. Abdolvand, "In-plane acoustic reflectors for reducing effective anchor loss in lateral–extensional MEMS resonators," *J. Micromech. Microeng.*, vol. 21, no. 8, p. 085021, 2011.

[23] J. Wang, J. E. Butler, T. Feygelson, and C. T.-C. Nguyen, "1.51-GHz nanocrystalline diamond micromechanical disk resonator with material-mismatched isolating support," in *Proc. 17th IEEE Int. Conf. Micro Electro Mech. Syst. Maastricht MEMS Tech. Dig.*, Jan. 2004, pp. 641–644.

[24] G. Casinovi, X. Gao, and F. AyaziLamb, "Lamb waves and resonant modes in rectangular-bar silicon resonators," *J. Microelectromech. Syst.*, vol. 19, no. 4, pp. 827–839, Aug. 2010.

[25] M. Ghatge, P. Karri, and R. Tabrizian, "Power-insensitive silicon crystal-cut for amplitude-stable frequency synthesis," in *Proc. IEEE 30th Int. Conf. Micro Electro Mech. Syst. (MEMS)*, Jan. 2017, pp. 76–79.

[26] R. Tabrizian and F. Ayazi, "Acoustically-engineered multi-port AlN-on-silicon resonators for accurate temperature sensing," in *IEDM Tech. Dig.*, Dec. 2013, pp. 18.1.1–18.1.4.

[27] A. Ansari, R. Tabrizian, and M. Rais-Zadeh, "A high-Q AlGaN/GaN phonon trap with integrated HEMT read-out," in *Proc. Transducers 18th Int. Conf. Solid-State Sens., Actuators Microsyst. (TRANSDUCERS)*, Jun. 2015, pp. 2256–2259.

[28] J. F. Rosenbaum, *Bulk Acoustic Wave Theory and Devices* (Artech House Acoustics Library). Norwood, MA, USA: Artech House, Jun. 1988.

[29] K. F. Graff, *Wave Motion in Elastic Solids*. North Chelmsford, MA, USA: Courier Corporation, 2012.

[30] W. Y. Yang, W. Cao, T.-S. Chung, and J. Morris, *Applied Numerical Methods Using MATLAB*. New York, NY, USA: Wiley, 2005.

[31] G. G. Fattinger, S. Marksteiner, J. Kaitila, and R. Aigner, "Optimization of acoustic dispersion for high performance thin film BAW resonators," in *Proc. IEEE Ultrason. Symp.*, vol. 2, Sep. 2005, pp. 1175–1178.

[32] G. G. Fattinger, "BAW resonator design considerations—An overview," in *Proc. IEEE Int. Freq. Control Symp.*, May 2008, pp. 762–767.

[33] R. Ruby, J. Larson, C. Feng, and S. Fazzio, "The effect of perimeter geometry on FBAR resonator electrical performance," in *Proc. Microw. Symp. Dig.*, Jun. 2005, pp. 217–221.

[34] R. C. Ruby, J. D. Larson, R. S. Fazzio, and C. Feng, "Performance degradation effects in FBAR filters and resonators due to lamb wave modes," in *Proc. Ultrason. Symp.*, vol. 3, Sep. 2005, pp. 1832–1835.

[35] R. Strijbos, A. Jansman, J.-W. Lobeek, N. X. Li, and N. Pulsford, "Design and characterisation of high-Q solidly-mounted bulk acoustic wave filters," in *Proc. 57th Electron. Compon. Technol. Conf.*, May/Jun. 2007, pp. 169–174.

Mayur Ghatge (S'17) received the bachelor's degree in electrical engineering from IIT Jodhpur, Jodhpur, India, in 2014. He is currently pursuing the Ph.D. degree with the Department of Electrical and Computer Engineering, University of Florida, Gainesville, FL, USA.

From 2014 to 2015, he was a Research Assistant with the Indian Institute of Science, Bengaluru, India. His current research interests include linear and nonlinear RF MEMS and micro-/nanofabrication technologies.

Roozbeh Tabrizian (S'06–M'14) received the B.S. degree in electrical engineering from the Sharif University of Technology, Tehran, Iran, in 2007, and the Ph.D. degree in electrical and computer engineering from the Georgia Institute of Technology, Atlanta, GA, USA, in 2013.

From 2014 to 2015, he was a Post-Doctoral Scholar with the University of Michigan, Ann Arbor, MI, USA. He is currently an Assistant Professor with the Department of Electrical and Computer Engineering, University of Florida, Gainesville, FL, USA. His research has resulted in more than 40 journals and refereed conference papers, and holds 16 patents and patent applications. His current research interests include linear and nonlinear microacoustic and nanoacoustic devices, RF micro-electromechanical systems (MEMS), mixed-domain nanosystems for time-keeping and transfer, frequency reference, and spectroscopy applications, and nanofabrication technologies.

Dr. Tabrizian was a recipient of the NSF CAREER Award in 2018. He and his students are the recipients of outstanding paper awards at the IEEE International Conference on Micro Electro Mechanical Systems (IEEE MEMS) and International Conference on Solid-State Sensors, Actuators, and Microsystems (Transducers).